JGR Space Physics

DATA ARTICLE
10.1029/2022JA030299

DMSP Poynting Flux: Data Processing and Inter-Spacecraft Comparisons

Liam M. Kilcommons[1], Delores J. Knipp[1], Marc Hairston[2], and W. Robin Coley[2]

[1]Ann and H.J. Smead Aerospace Engineering Sciences, University of Colorado, Boulder, CO, USA, [2]William B. Hanson Center for Space Sciences, University of Texas, Dallas, TX, USA

Key Points:

- We describe the data processing for a new Poynting flux (PF) database and provide code access
- We provide an inter-comparison of PF from three Defense Meteorological Satellite Program Spacecraft via a conjunction analysis
- Use of all electric field components to calculate PF significantly improves the inter-comparison

Correspondence to:

D. J. Knipp,
delores.knipp@colorado.edu

Citation:

Kilcommons, L. M., Knipp, D. J., Hairston, M., & Coley, W. R. (2022). DMSP Poynting flux: Data processing and inter-spacecraft comparisons. *Journal of Geophysical Research: Space Physics*, *127*, e2022JA030299. https://doi.org/10.1029/2022JA030299

Received 18 JAN 2022
Accepted 5 JUL 2022

Author Contributions:

Conceptualization: Liam M. Kilcommons, Delores J. Knipp
Data curation: Marc Hairston, W. Robin Coley
Funding acquisition: Delores J. Knipp
Methodology: Liam M. Kilcommons
Project Administration: Delores J. Knipp
Software: Liam M. Kilcommons
Supervision: Delores J. Knipp
Visualization: Liam M. Kilcommons
Writing – original draft: Liam M. Kilcommons, Delores J. Knipp
Writing – review & editing: Liam M. Kilcommons, Delores J. Knipp, Marc Hairston

Abstract Poynting flux (PF) calculated from low Earth orbit spacecraft in situ ion drift and magnetic field measurements is an important measure of energy exchange between the magnetosphere and ionosphere. Defense Meteorological Satellite Program (DMSP) spacecraft provide an extensive back-catalog of ion drift and magnetic perturbation measurements, from which quasi-steady PF could be calculated. However, since DMSP are operations-focused spacecraft, data must be carefully preprocessed for research use. We describe an automated approach for calculating earthward PF focusing on pre-processing and quality control. We produce a PF data set using nine satellite-years of DMSP F15, F16, and F18 observations. To validate our process we inter-compare PF from different spacecraft using more than 2,000 magnetic conjunction events. We find no serious systematic differences. We further describe and apply an equal-area binning technique to obtain average spatial patterns of PF, magnetic perturbation, electric field and ion drift velocity. We perform our analysis using all components of electric and magnetic field and comment on the adverse consequences of the typical single-electric-field-component DMSP PF approximation on inter-spacecraft agreement. Including full-field components significantly increases the relative strength of near-cusp PF and increases the integrated high-latitude PF by ~25%.

Plain Language Summary We describe the processing of observations from approximately 45,000 Defense Meteorological Satellite Program spacecraft orbits over the course of 3 yr, which can be used to study the climatology of electromagnetic energy transfer (also known as Poynting flux [PF]) between the magnetosphere and ionosphere. Observations from three instruments on three operational spacecraft are used to produce the necessary estimates of electric field and magnetic field perturbations that go into the PF calculation. Our processing pipeline includes data checking, baseline removal, and spatial binning of electric and magnetic field perturbations to produce maps of the individual elements of PF. We bin the results in equal-area bins for each hemisphere. To verify our work, we provide comparisons of individual measurements made by different spacecraft when they are close to each other in space and time. In general, we find the best agreement when we use all components of available field data. Including full-field components significantly increases the relative strength of near-cusp PF and increases the integrated high-latitude PF by ~25%.

1. Introduction

Episodic orbit-perturbing events of the early space age (e.g., February 1958, July 1959, and November 1960) produced several lines of inquiry about their root causes. Jacchia (1959a, 1959b) first proposed variations in solar shortwave energy and then "corpuscular" deposition associated with magnetic storms as sources, while Dessler (1959) advocated for hydromagnetic wave heating. Availability of early solar wind data led Cole (1966) to assert that variation in storm-time energy deposition in the thermosphere arising from solar wind magnetosphere interactions was the likely dominant source of episodic low Earth orbit (LEO) perturbations and enhanced satellite drag. An early NASA mission, Injun-5/Explorer-40, indicated that very low frequency electromagnetic energy transfer was predominantly earthward at plasmaspheric altitudes (Mosier & Gurnett, 1969). Quantifying the electromagnetic energy transfer (now often referred to as "Poynting flux") between the magnetosphere and ionosphere has been challenging during the last half century due to the need for in situ coincident measurement of magnetic and electric fields and their variation. We discuss the data processing required to take advantage of the Defense Meteorological Satellite Program (DMSP) coincident measurements of ion drift and magnetic field to calculate quasi-steady Poynting flux (PF).

Table 1
Data Sources for Raw Data, "Madrigal" Refers to the CEDAR Madrigal Database, and "CDAWeb" Refers to NASA Coordinated Data Analysis Web

Spacecraft	Years	SSIES	SSM
F15	2011–2013	Madrigal	CDAWeb
F16	2012–2014	CDAWeb	CDAWeb
F18	2012–2014	CDAWeb	CDAWeb

Estimates of Alfvénic (wave) and quasi-steady PF have been produced from LEO and beyond starting in the late 1960s. Recently Kaeppler et al. (2022) reviewed the PF literature and provided summaries of mission results from dozens of studies. Their Table 1 shows reported typical quasi-steady PF values of 1–10 mW/m^2 near the dayside cusp and auroral zones of both hemispheres (mapped to approximately 100 km). Originally the maps of quasi-steady PF were rather coarse with only enough data for averaging over both hemispheres (Gary et al., 1995; Olsson et al., 2004). Both of these studies showed the intensity and areal coverage of PF deposition increased with increasing geomagnetic activity. Empirical, combined-hemisphere models of quasi-steady PF have been developed (e.g., Cosgrove et al., 2014; Weimer, 2005) and binned by the interplanetary magnetic field (IMF) and solar wind conditions.

During the last decade, a growing archive of DMSP data has supported investigation of intense PF deposition into both hemispheres. Huang et al. (2017) found values of PF exceeding 100 mW/m^2 in the dawn regions of both hemispheres during a few of the main phases of the 30 geomagnetic storms they studied, however, most high-latitude storm time values were less than 20 mW/m^2. Knipp et al. (2011) reported similar large values in the near-cusp region of both hemispheres during intervals when the IMF B_y component was large. Some of these studies used only the cross-track ion drift to compute the electric field contributing to PF due to concerns about the quality of the along-track ion drift data.

Improvements in DMSP data processing allowed Knipp et al. (2021) to provide quasi-steady PF maps at 220 km resolution for both hemispheres using all electric field components. As in earlier studies, they showed intensity and areal coverage of PF deposition scaled with increasing activity. They also showed that, consistent with previous reports by Pakhotin et al. (2021) for Alfvénic PF, there is a clear preference for excess northern hemisphere deposition of PF. Billett et al. (2022) and Cosgrove et al. (2022) recently confirmed the northern hemispheric PF preference in re-processed Fast Auroral Snapshot data and Swarm data, respectively. The present paper provides more detail about the processing and inter-comparison of spacecraft data that support the multiyear analysis in Knipp et al. (2021) and will support future research. We provide links to the raw data, the reduced data, and supporting software. In Section 2, we discuss data quality flags and binning methods as well as ion-drift baseline removal. In Section 3, we demonstrate good agreement of the derived PF between spacecraft during magnetic conjunction events. We also quantify the improvement in PF obtained by using full-component electric field data. We conclude in Section 4.

2. Methods and Data

Knipp et al. (2021) provided independent maps of quasi-static PF in each hemisphere based on nine satellite-years of DMSP data. The detailed creation of the data set used in that publication will be described herein. Spatial binning was executed to conserve spatial resolution at lower latitudes by using bins of 2° latitude on a side (220 km) and a width in Magnetic Local Time (MLT) that produces a square-surface area for each bin. Each hemisphere has 1,151 equal-area bins. To aid future researchers in understanding or reproducing our results, we use only publicly available data, and make our software available via Github.

2.1. Data

The DMSP data sets are the Level-2 special sensor magnetometer (SSM) magnetometer data set described in Kilcommons et al. (2017) and the special sensor for ions electrons and scintillations 3 (SSIES3) ion drift and plasma parameters data set and the SSIES2 data set. Temporal coverage for the project is shown in Table 1. The F15 SSIES2 data from Madrigal was accessed via Pysat (Stoneback et al., 2018).

2.2. Ephemeris

The accuracy of spacecraft locations provided for DMSP spacecraft differs depending on the data source. For this study, we use the reprocessed spacecraft positions extracted from the DMSP magnetometer data files, as

described in Kilcommons et al. (2017). These ephemeris are derived from those distributed by the NASA Satellite Situation Center Web (SSCWeb) spacecraft locator service. All magnetic coordinates reported herein are Modified Magnetic Apex (Emmert et al., 2010; van der Meeren et al., 2021) locations using a reference altitude of 110 km.

2.3. Software and Data Processing Pipeline

The data processing pipeline was written in Python under Git version control using best practices such as unit testing, PEP8 style, logging, and configuration files. The purpose of the pipeline is to produce two types of data. First, we have produced orbit-by-orbit NASA Common Data Format (CDF) files which contain all of the parameters required to calculate PF. Second, by applying our equal-area binning approach, we have produced a binned data product in Hierarchical Data Format Version 5 (HDF5) format. The orbit-by-orbit files represent vectors (fields, ion drift) and PF in spacecraft frame, whereas the binned data products use magnetic coordinates (see Section 2.5).

2.3.1. Orbit-By-Orbit Data

These files are created by first reading SSIES data from various source formats. Then the baseline correction for the ion drift measurements is performed. Then, the appropriate SSM data is added aligning the timestamps to produce a merged NASA CDF data file. Finally, electric field and PF are calculated. Each such file covers one full DMSP orbit for one spacecraft.

2.3.2. Binned Data

This process begins by reading each CDF output file, calculating field-aligned PF (and other electrodynamic parameters) and organizing the data into bins in magnetic coordinates. The result is a single HDF5 output file organizing all individual PF data points by bin. We provide the software which defines the equal-area bins and the HDF5 file format as an open-source Python library called esabin (see Data Availability Statement). The data products produced by this workflow (as used in this study and in Knipp et al., 2021) have been published on Zenodo (see Data Availability Statement).

2.4. Magnetometer Data

The DMSP SSM measures the three orthogonal components of the magnetic field at the spacecraft and reports average values at 1 s cadence. Post-processing corrects and/or verifies the location of the spacecraft based on ground-tracking information and then calculates the appropriate International Geomagnetic Reference Field, $\mathbf{B}_0$ and removes it to yield the perturbation field, $\delta\mathbf{B}_M$. A further baseline correction intended to remove instrument artifacts and low-latitude perturbations correlated with the ring current is performed (Rich et al., 2007). This baseline signal for each $\delta\mathbf{B}$ component is found by first dividing measurements acquired during each half orbit into three segments: the first two extend from the equator to the low-latitude auroral boundaries on the evening and morning sides while the remaining segment encompasses the aurora and polar cap where most magnetic perturbations are found.

Auroral and polar cap boundaries are identified via automated inspection of variations of precipitating particle fluxes detected by the DMSP particle sensor. Then least squares polynomial fits are applied to each of the components of $\delta\mathbf{B}$ using the data from the subauroral segments. Baseline values of the three components are then extended via calculated polynomials across high-latitude segments to obtain $\mathbf{B}_{Fit}$ from equator to equator along entire half orbits. The corrected magnetic perturbation vectors used in this study are then calculated as $\delta\mathbf{B}_C = \delta\mathbf{B}_M - \mathbf{B}_{Fit}$. This process is described in detail in Kilcommons et al. (2017).

2.5. Coordinate Frames for Vector Quantities

It is important to note that the naming convention for directions in the spacecraft body-fixed coordinate frame used for DMSP SSM differs from that used for SSIES. For SSM the convention is $\hat{x_m}$ is geodetic downward (nadir), $\hat{y_m}$ perpendicular to $\hat{x_m}$ in the plane of the spacecraft velocity vector, and $\hat{z_m}$ completes the right-handed frame. For SSIES, $\hat{x}$ is parallel to the spacecraft velocity vector, $\hat{z}$ is geodetic upward (zenith), and $\hat{y}$ completes

the right-handed frame. In all calculations that follow we use the latter (SSIES) convention. In the case of vector quantities in magnetic coordinates, Modified Magnetic Apex unit vectors are used as suggested in as in Laundal and Richmond (2017). That is, we use the d basis for field measurements and the e basis for ion drift velocity.

2.6. Processing for Ion Drift Data

Automated quality control is essential in a reproducible data processing scheme. Previous work by Kilcommons et al. (2017), summarized above automated quality control for the SSM magnetometer. In this work, we introduce an automated quality control procedure for the SSIES ion drift.

2.6.1. Quality Flags

Several variants of SSIES data are available in public archives. The SSIES data products used here include University of Texas Dallas (UTD) quality flags as described in Hairston and Coley (2019). The UTD quality flags are integer values which accompany each ion drift datapoint. Quality "1" data is useable, and quality "2" data may also be useable. Larger quality flag values' meanings are detailed in the guide referenced above. The quality flags are assigned independently to each of the two sensors which measure ion drift. The ion drift meter (IDM) measures in the vertical (zenith) and cross-track (perpendicular to zenith and spacecraft velocity vector) directions. The retarding potential analyzer (RPA) measures in the ram direction (parallel to the spacecraft velocity vector). The quality flags are calculated using in situ -sensed or derived plasma parameters using IDM, RPA, and other sensors in the SSIES instrument package.

In general, our processing uses only quality "1" data. There is one exception to this requirement; the quality flags for version 2 SSIES (on the F15 spacecraft) are more conservative, only producing RPA quality "1" for a few points each orbit. Therefore we include quality "2" for version 2 of the SSIES (F15). Since no quality flagging algorithm can get every possible bad data point, we entirely discard any pass which has less than 40% quality 1 data for IDM or less than 30% quality 1 data for RPA.

2.6.2. Baseline

Another aspect of the SSIES ion drift data which is not addressed by the quality flags is a slow variation in the total value of the RPA and IDM drifts, such that the plasma drifts that change on the order of tens-to-hundreds of kilometers appear to overlay a smoother trend which varies over distances on the order of a quarter-to-half orbit. We will call the smoother trend the baseline. The baseline is not the co-rotation drift, as the ion drift variables in the SSIES data files mentioned in Table 1 already include this correction. Typically the baseline is treated by supposing that the drift should be near zero at mid-to-low latitude and shifting the data for each half-polar-orbit (from equator across pole to equator).

Our baseline approach is modeled after this typical method. We characterized the baseline on a "pass-by-pass" basis considering only the data poleward of 40° magnetic latitude (MLAT). In this context, a "pass" is half of one orbit (the data from one orbit, for either the northern or southern hemisphere). We model the baseline as a simple line ($y = a * t + b$), with time since the spacecraft crossed 40° MLAT traveling toward the pole as the t coordinate, and ion drift as the y coordinate. We use weighted least squares to determine the coefficients, with weights:

$$w(t) = \frac{1}{Q(t)^2} \frac{90 - |\lambda_m(t)|}{40} \tag{1}$$

with $Q(t)$ as the quality of each ion drift data point, and $\lambda_m(t)$ as the MLAT of the spacecraft. The rationale is to minimize the influence of poor quality drift data (leftmost ratio) and of higher latitude ionospheric drifts (rightmost) on the baseline.

Figure 1 shows the application of this technique using one orbit of F18 data. Baseline fits are individually calculated for each vector component and hemisphere. The resulting linear equations are shown.

Note any mention of ion drift data hereafter refers to "baseline-corrected" data, meaning the baseline has been fit and subtracted.

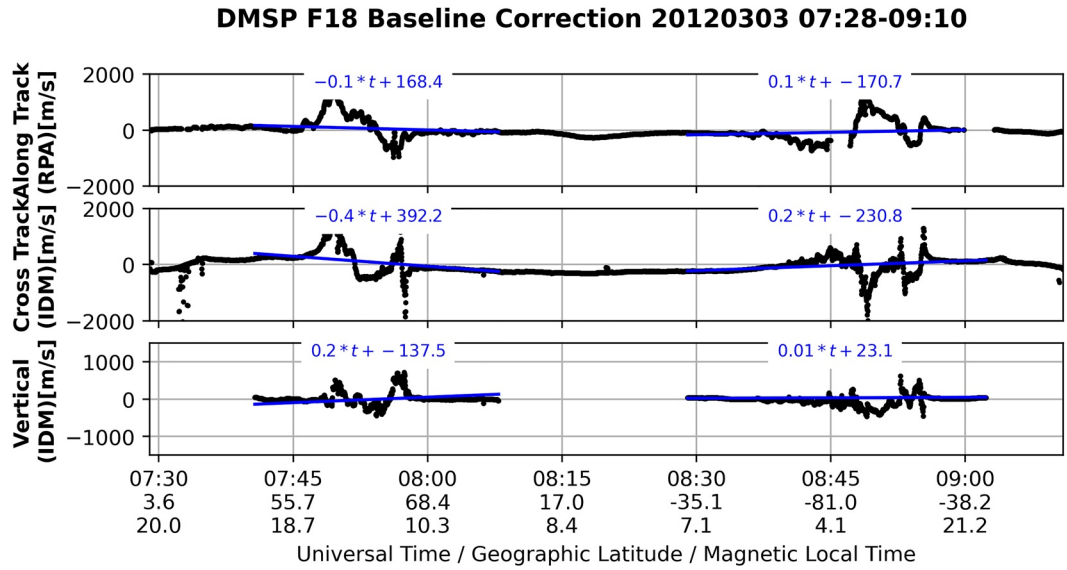

Figure 1. Example baseline correction for one full orbit (two passes) of F18 on 3 March 2012. Black curves are ion drift velocity, the baseline fits are shown in blue.

2.7. Electric Field Calculation

Electric field is calculated using the magnetic field measurements from SSM, and the ion drift measurements from SSIES as shown in Equation 2.

$$\vec{E} = -\vec{v}_{ions} \times \vec{B} \tag{2}$$

The components of this equation expand as:

$$E_x = v_z B_y - v_y B_z \tag{3}$$

$$E_y = v_x B_z - v_z B_x \tag{4}$$

$$E_z = v_y B_x - v_x B_y \tag{5}$$

Since the ram (v_x) and cross-track (v_y, v_z) drift velocities are measured by different instruments, we only calculate electric field when both instruments' data are both available and are of acceptable quality. Also, it is important to note that $B_z \gg B_x, B_y$ for polar regions because the geomagnetic field is nearly aligned with geodetic vertical.

2.8. PF Calculation

We begin by calculating the perturbation Poynting vector (in spacecraft frame) using the magnetic perturbation defined in Section 2.4:

$$\vec{S} = -\frac{1}{\mu_0} \vec{E} \times \delta\vec{B} \tag{6}$$

where μ_0 is the permeability of free space.

PF is typically defined as the component of the Poynting vector parallel to the geomagnetic main field. This is often approximated as the PF in the vertical (or radial) direction:

$$S_z = \vec{S} \cdot \hat{z} \tag{7}$$

where $\hat{z}$ is a unit vector in the geodetic upward (zenith) direction.

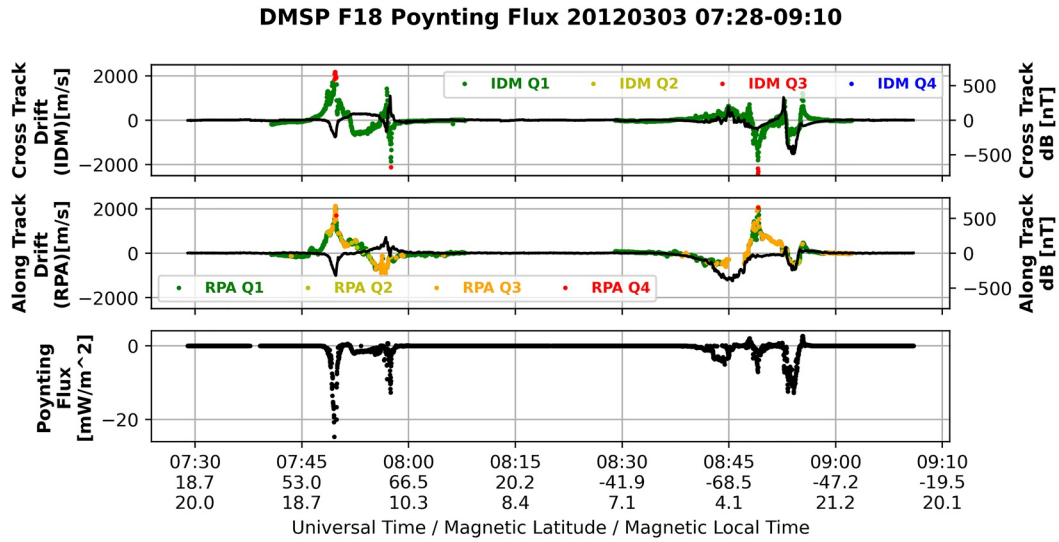

Figure 2. Example Poynting flux (PF) calculated for one full orbit (two passes) of F18 on 3 March 2012. Ion drift is shown colored by associated quality flag with green indicating good quality. Magnetic perturbations are shown in black. PF was calculated using only high-quality (green) ion drift.

We do not use this approximation, and instead follow Olsson et al. (2004) and compute the field-aligned PF into the ionosphere, scaling to an altitude of 110 km:

$$S_B = \frac{|\vec{B}_{110}|}{|\vec{B}_0|} \frac{\left(\vec{B}_{110} \cdot \hat{z}\right)}{|\vec{B}_{110}|} \left(\mp \hat{b}_0 \cdot \vec{S}\right) \tag{8}$$

where $\vec{B}_0$ is the International Geomagnetic Reference Frame (IGRF) at spacecraft location, $\hat{b_0}$ is a unit vector in the direction of $\vec{B}_0$, $\vec{B_{110}}$ is $\vec{B}_0$ at an altitude of 110 km. The sign in front of $\hat{b_0}$ ensures the flux is directed into the ionosphere in both northern (negative) and southern (positive) hemispheres. Note that the term $\left(\cos I = \frac{\left(\vec{B}_{110} \cdot \hat{z}\right)}{|\vec{B}_{110}|}\right)$ is nearly unity (ranging from 0.94 to 1.00) for mid-to-high MLATs ($|\lambda_m| > 60$).

Figure 2 shows ion drift and magnetic perturbations measurements and the resulting PF for the same F18 orbit as Figure 1.

2.9. Spatial Binning and Statistics

Many studies calculating PF from in situ electromagnetic measurements have used spatial binning in magnetic coordinates to understand where and under what conditions strong PF occurs. Most authors use MLAT and MLT to define their bins. For instance, all bins might be 3° in latitude by 1 hr MLT. However, considered as sections of the surface of a sphere, constant latitude/MLT bins produce severely biased sampling: the area of a bin at mid-latitudes is an order of magnitude greater than the area of a bin near the pole.

We use an alternative approach, in which bins have a constant latitude width, but the width in MLT varies with latitude to approximate equal surface area for each bin. The top row of Figure 3 shows binned data from passes in the northern and southern hemispheres. This approach introduces complications for how the data is stored. For reproducibility, our open-source software package (esabin) which implements both this approach and the constant MLT approach above is available on Github.

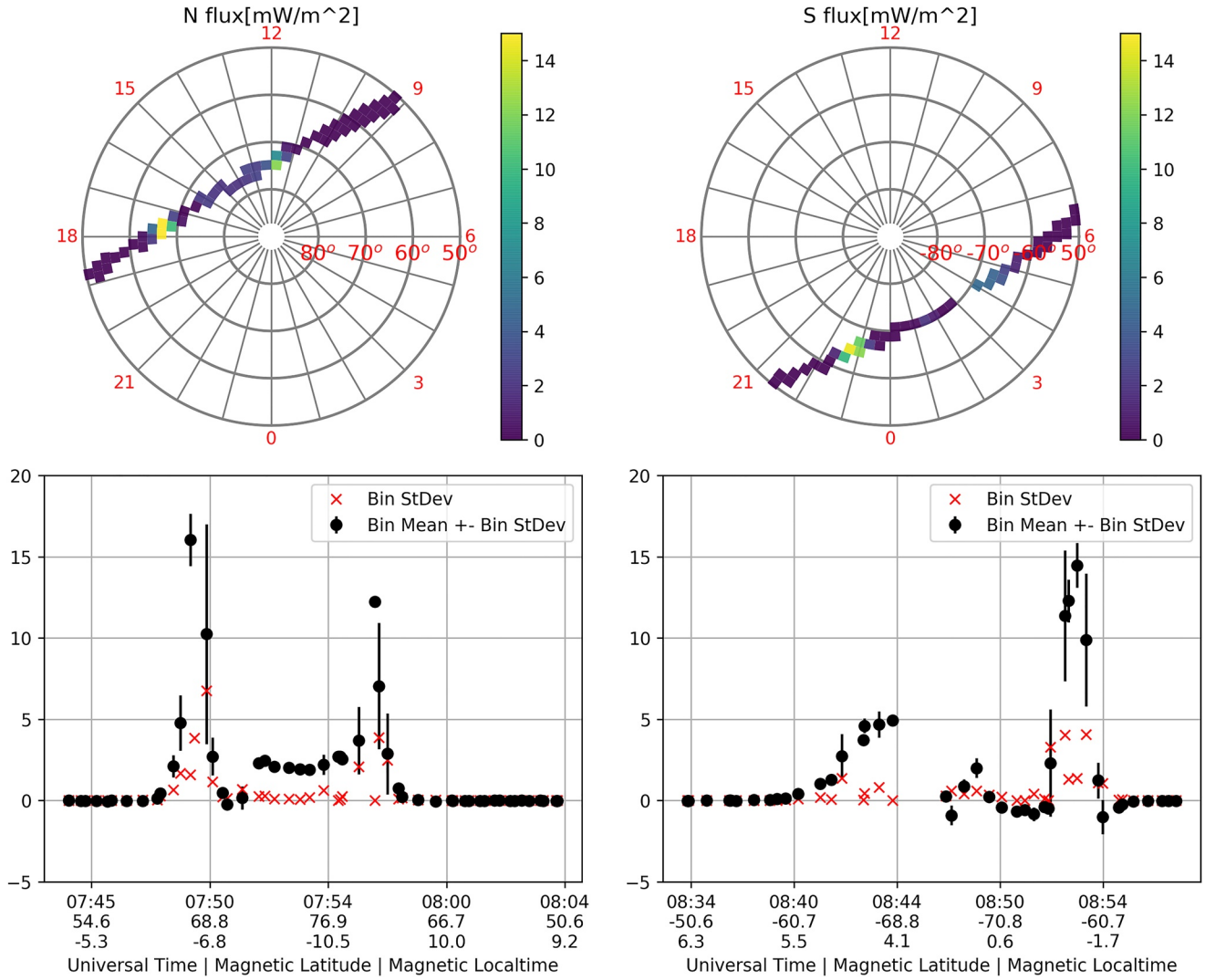

Figure 3. Binned and reduced Poynting flux (PF) for previously shown orbit of F18 on 3 March 2012. Northern hemisphere PF is in the left column while southern hemisphere PF is in the right column. Color in polar plots indicates downward PF magnitude, matching black curve in line plots. Error bars and red "*x*" markers in line plots represent sub-bin-scale variability as quantified by the standard deviation of 1 s measurements in bin. Missing dawn-sector bins in top right due to localized quality drop in ion drift measurements.

2.9.1. Binning Procedure

Another practical consideration for this study was how to store and retrieve the binned data. The amount of data from multiple spacecraft years of high-cadence (F15: 4 s sampling, F16, and F18: 1 s sampling) data is very large and cannot be stored easily in memory (RAM) on a typical desktop computer.

We devised a two step solution to this problem. The first step is to reorganize the data into individual crossings of particular bins, and store this new data set in a file, instead of in RAM. This new data set is a HDF file with a Group for each bin. The HDF format allows data to be written to any Group at any time, so it becomes feasible to store the entire multiyear, multi-spacecraft data set in one file by adding the data one orbit at a time. The result is that each bin's Group is filled with data sets, each representing one spacecraft crossing that bin at one specific time. Each such data set contains around 15 samples of 1 s data, or around four samples of 4-s data. Also each data set stores additional metadata, most importantly the date and time of the crossing and the "F-number" of the spacecraft (e.g., F15). The resulting file is very large and preserves every data point of the original data.

The second step is to further reduce the data size by considering each bin crossing (each data set in the HDF file) as one "sample" of the spatial area of that bin and storing only the mean and standard deviation of the data from

that bin crossing. In addition to making the data smaller, this also "standardizes" the data (for instance, removing any need to take the 4 s vs. 1 s sampling into account).

After the two-step reduction process, the data from each bin is much more easily manipulated. For instance, the average of the reduced data, for each bin, for several electrodynamic parameters is shown in Figure 4. For vector quantities, separate HDF files are created, reduced, and averaged for the geomagnetic eastward and northward components, and then the average of each component for each bin is used to create the vector plots.

2.10. Spacecraft Inter-Comparisons

Occasionally, two spacecraft fly through nearly the same region of space at nearly the same time. Previous studies (Knipp et al., 2014, 2015) termed this event a "magnetic conjunction." In contrast to a physical conjunction, which is a collision of two orbiting objects, a magnetic conjunction is an interval of time where two spacecraft were nearly co-located in magnetic coordinates ("on the same field line"). To find magnetic conjunctions using our data, we searched each bin Group from the aforementioned HDF5 files for samples from different DMSP spacecraft which occurred within 90 s of each other. We then compared the bin-average PF measured by each spacecraft to determine the degree of agreement. Using bin-average values allows us to compare primarily large scale (comparable to the bin size) structures, which are thought to vary more slowly than those with smaller scale sizes (e.g., Knipp et al., 2015).

3. Results and Discussion

The data processing described in previous sections is an extension and improvement of that used in Rastätter et al. (2016) who reported a PF uncertainty of approximately 2.5 mW/m^2 using the good quality DMSP data. Recognizing that "ground truth" for direct comparisons of PF could only come from estimates made by incoherent scatter radars, we try a different approach of inter-spacecraft comparison described below.

3.1. Spacecraft Inter-Comparisons

Figure 5 shows comparisons (as scatterplots) of bin-average PF between each pair of DMSP spacecraft for more than 2,000 such events. For all pairs of spacecraft, the PF measured is highly correlated (Spearman correlation (ρ) of 0.7 or higher). The trendline fits (calculated using a median-based robust regression) all have slopes close to 1, and large R^2 (coefficient of determination) values. This indicates all spacecraft measure the same large-scale PF for the majority of conjunctions, to within some amount of scatter. The lower right element of the figure summarizes the three inter-comparisons as box-and-whisker plots for small (<5 mW/m^2) and large (>5 mW/m^2) values of PF. The quantity plotted is percent difference in PF:

$$\Delta S_B = \frac{S_{B,1} - S_{B,2}}{\left(\frac{S_{B,1} + S_{B,2}}{2}\right)} * 100 \tag{9}$$

The box-and-whisker plots show median as the black horizontal line, with the box edges at 25th and 75th percentile. The whiskers are median $\pm$1.5*(inter-quartile range). The leftmost three boxes apply to conjunctions where the average PF (mean of the flux from the two spacecraft) was nearly negligible (less than 5 mW/m^2), while the rightmost three boxes indicate conjunctions with non-negligible flux (average > 5 mW/m^2). Concentrating on the larger PF values, slightly more systematic difference is seen for comparisons involving F15 (blue and red), with median percent difference of approximately -30% (-28% for F15/F16%, -31% for F15/F18). F15 carries the earlier generation of ion drift instrumentation (SSIES2) which operates at a lower temporal cadence (0.25 Hz) and produces less quality 1 data. Considering only spacecraft equipped with the newer SSIES3 drift instruments (F16 and F18) the median percent difference is -13%, indicating very good agreement.

3.2. Full Electric Field Vs. Single Component Approximation

Many previous studies computing DMSP PF have used only one component of the electric field (E_x in Equation 5), derived from the across track (y direction) component of the ion drift velocity, and assuming all other velocity components are zero. The rationale for this is the along-track component of ion drift is measured by a

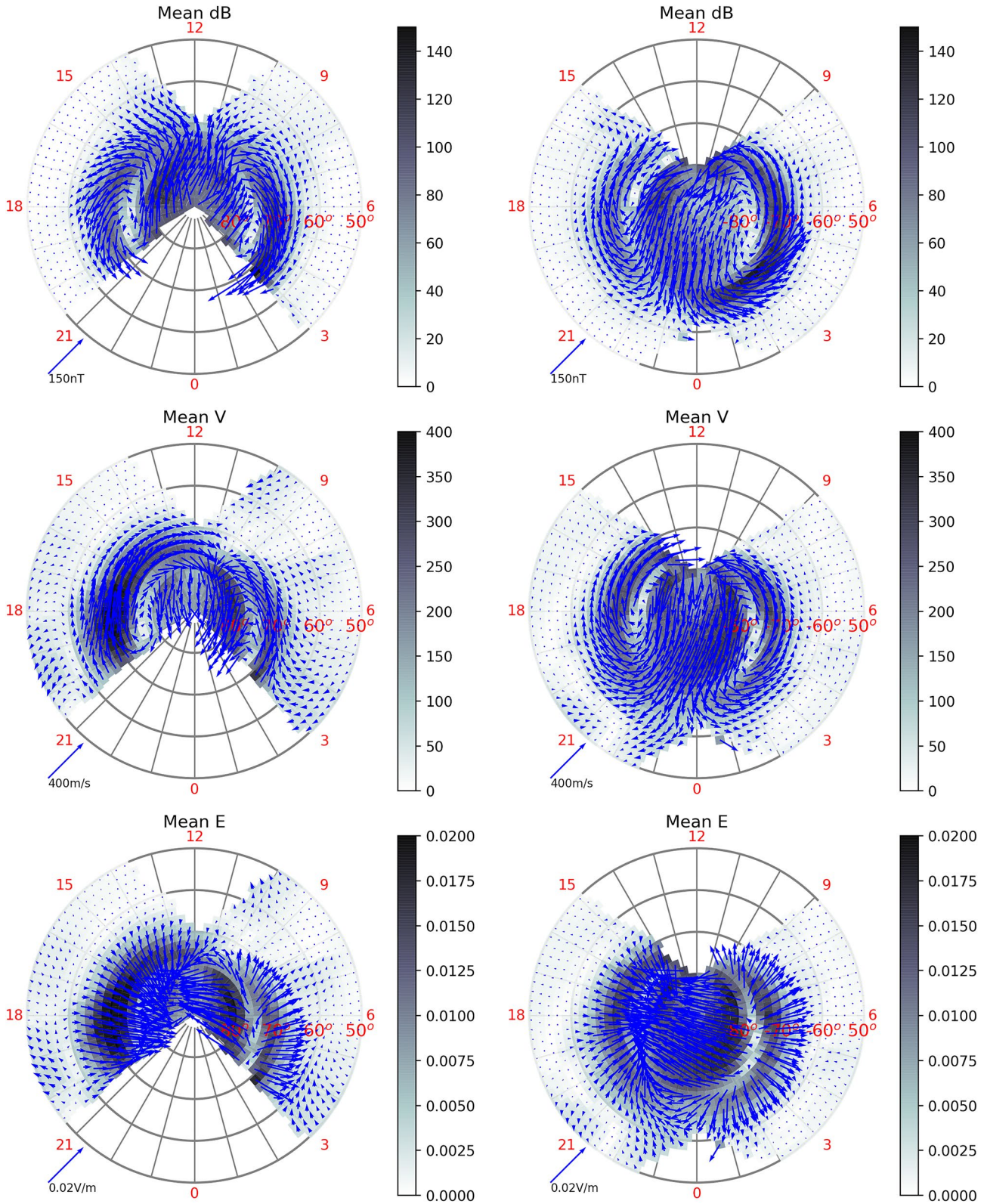

Figure 4. Electrodynamic vector parameters binned into equal area bins (each 2° wide in latitude). The top row shows average magnetic perturbations; the middle row shows average ion drift vectors and the bottom row show average electric field vectors. Northern (southern) hemisphere is on the left (right). Shading shows the vector magnitude.

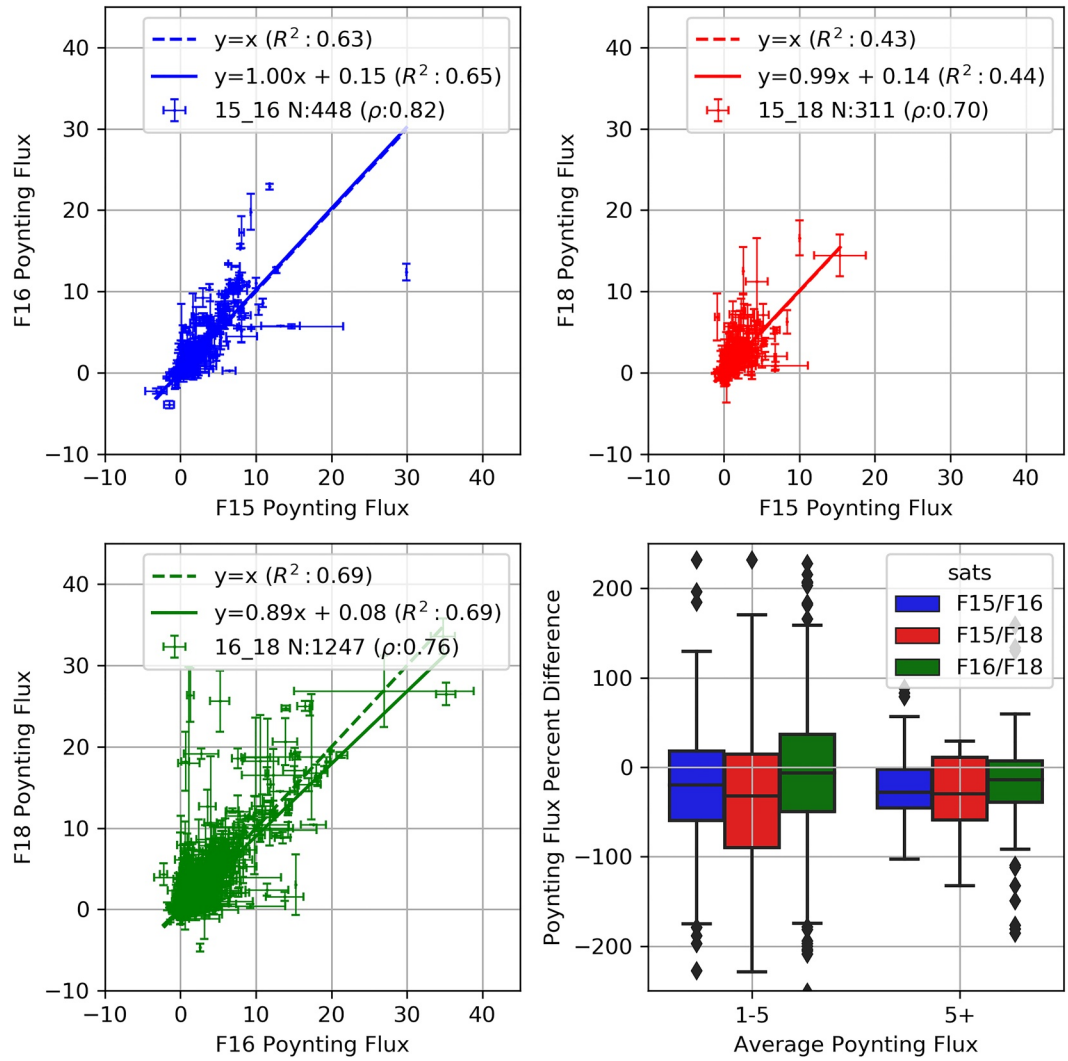

Figure 5. Poynting flux (PF) $\left(\frac{mW}{m^2}\right)$ measured by each spacecraft involved in a magnetic conjunction. Top left, top right, and bottom left panels show the bin-average PF for each magnetic conjunction between each pair of Defense Meteorological Satellite Program (DMSP) spacecraft, with error bars representing the bin standard deviation. The vertical error bars correspond to the spacecraft on the *y*-axis, and the horizontal error bars the spacecraft on the *x*-axis. Dashed lines represent the "perfect match" line ($y = x$). Solid lines show the robust (Theil-Sen) linear fit to the data. Coefficient of determination (R^2) is shown for both lines. Lower right panel shows the percent difference of PF measured by each spacecraft pair during magnetic conjunctions.

different instrument (the RPA) which produces noisier velocity data and has more missing values. We are able to eliminate this approximation because we are using an improved version of the SSIES 3 data (see Table 1), and because our spatial bin-and-average reduces the effect of the RPA noise. Note that we have used the full PF throughout this manuscript, except for the comparison in this section.

3.2.1. Effect on Inter-Spacecraft PF Consistency

To illustrate the difference between single and full component PF, Figure 6 shows the results of the magnetic conjunction analysis of Figure 5 using the single component approximation. For all 3 pairs of spacecraft, the line which approximates the average trend of the conjunctions does not have a slope close to 1, meaning on average the PF measurements are not consistent. The correlations are also reduced and the percent differences are larger with median values which are not as close to zero.

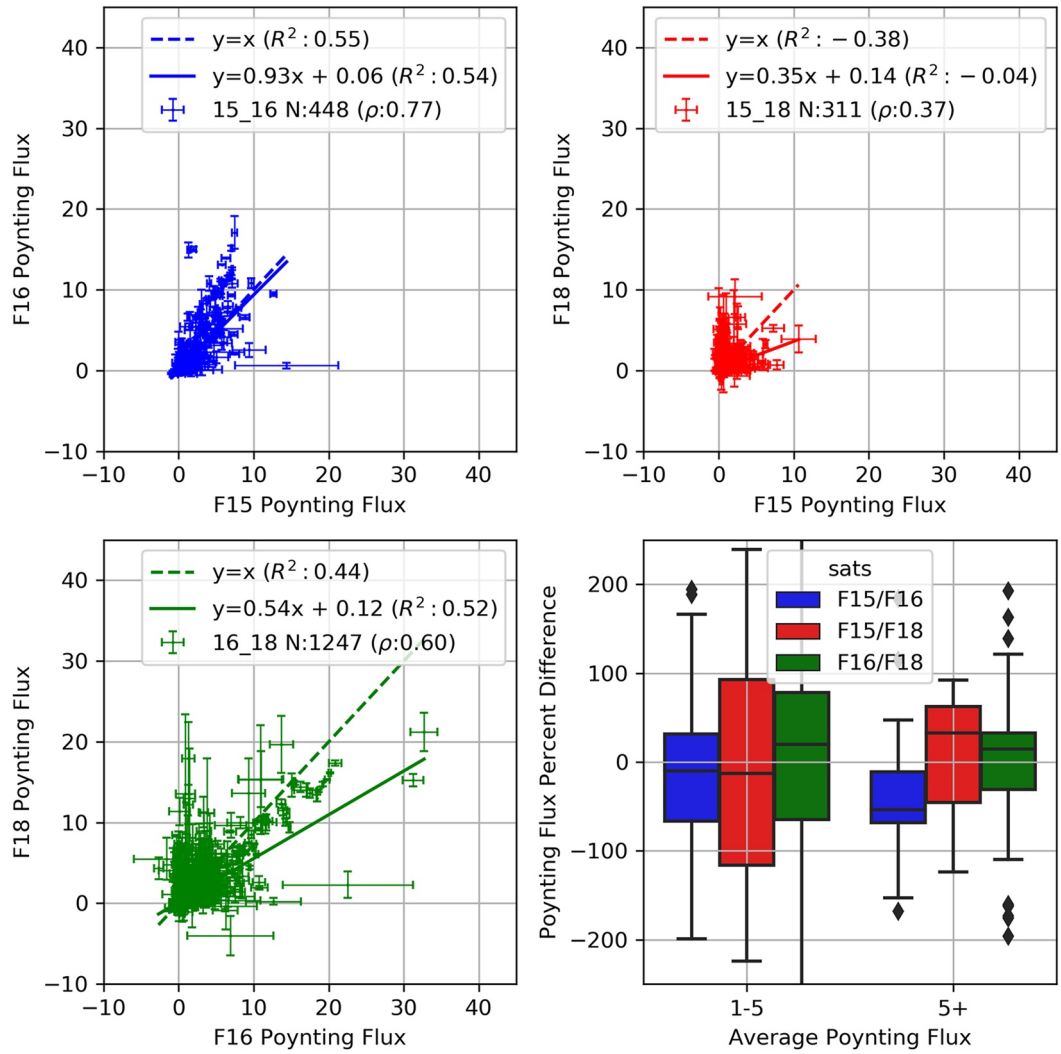

Figure 6. Poynting flux $\left(\frac{mW}{m^2}\right)$ calculated using only one component of the electric field (derived from the cross-track [IDM] velocity, with along-track and vertical velocities assumed 0) measured by each spacecraft involved in a magnetic conjunction (identical to Figure 5).

3.2.2. Effect on Spatial PF Pattern

With an eye to the degradation of the conjunction analysis results using single component PF, Figure 7 shows the resulting average spatial pattern of ion drift and PF. Unsurprisingly, there is overall less PF in the single component approximation, but importantly, there is significantly reduced PF in the noon high latitude (near-cusp) in the IDM-only view, even when accounting for the overall reduction. Specifically, the integrated PF in the northern hemisphere day (8–16 MLT) sector drops from 11.3 to 6.8 GW (40%) between full and single component variants. In contrast, the integrated flux from the remaining northern hemisphere bins drops only 20% (20.6–15.9 GW). See Table 2 for a summary. This indicates that previous studies using single-component PF could underestimate the relative importance of this region. Comparing the ion drift (the top 4 panels of Figure 7) suggests an explanation: the direction of ion flow in the near-cusp region is highly spatially variable, bending from sunward in the lower latitude to anti-sunward across the polar cap, and effect which is largely missed in the IDM-only picture. Moreover, the near-cusp flow is known to be particularly dynamic (for instance, the movement of the convection throat in response to changing IMF B_y). The spatial pattern of the average magnetic perturbations also bends in a similar manner (Figure 4) and we have verified it too is dynamic and sensitive to the direction of IMF B_y (not shown). Thus a missing electric field component is particularly problematic for resolving PF in this region.

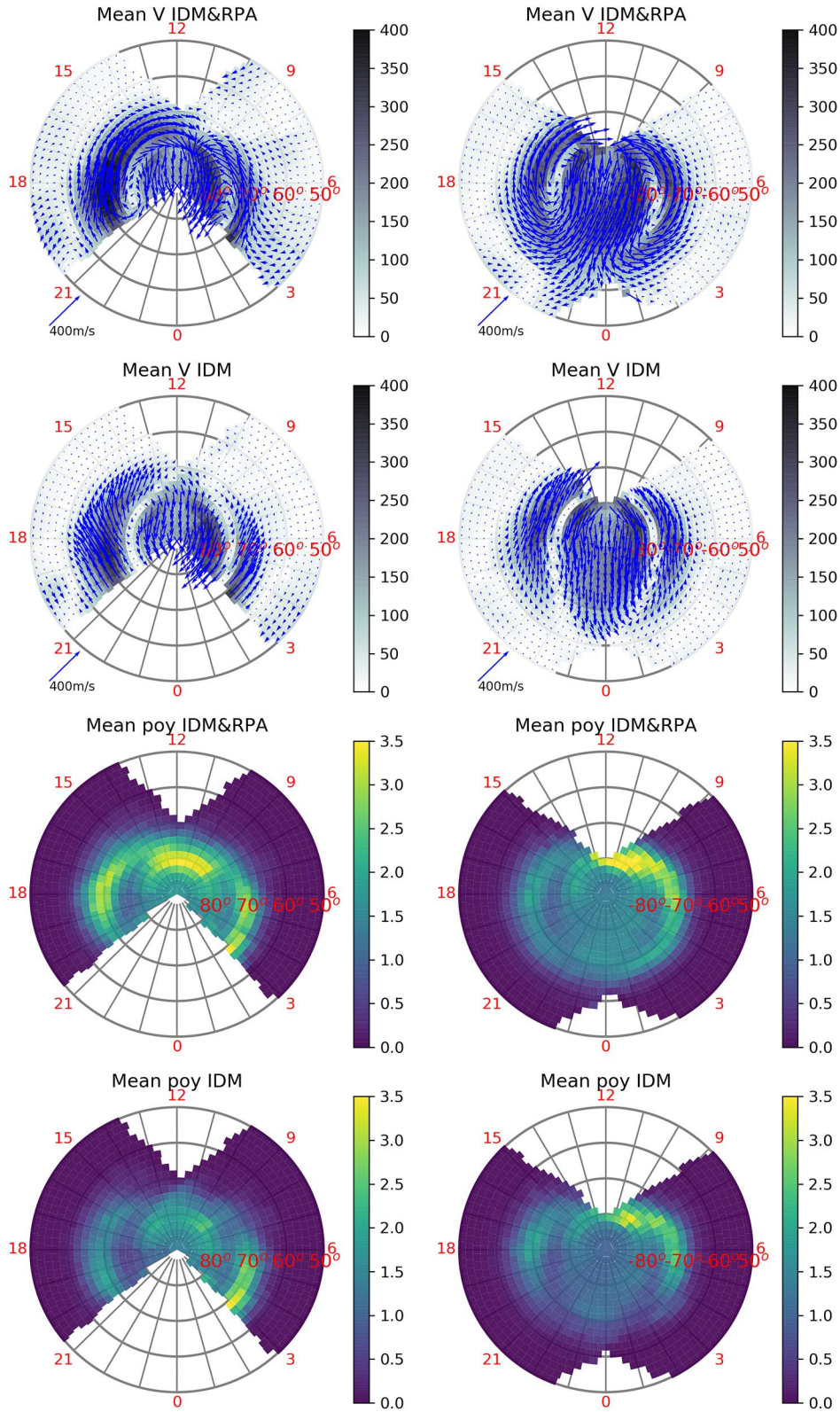

Figure 7. Spatial patterns of ion drift and Poynting Flux (PF). The top row shows ion drift determined from along- and cross-track drifts. The second row shows only cross-track drift. The PF in the third row corresponds to the full drift component electric field. The bottom plots show PF calculated from only the cross-track (IDM) ion drift velocity. Northern hemisphere patterns are on the left and southern on the right.

Table 2
Integrated Bin-Average Northern Hemisphere Poynting Flux (GW; as Shown in Figure 7)

Instrument	Total	MLT 8–16	MLT 16–24, 0–8
IDM	22.8	6.8	15.9
IDM + RPA	31.9	11.3	20.6

4. Conclusions

We describe recent improvements to DMSP ion-convection data products that are incorporated into producing the nine spacecraft-years of DMSP PF reported in Knipp et al. (2021). With the descriptions provided herein, we make the data processing routines and processed data available for general use. These improvements, which are applied to observations from three DMSP spacecraft, include an automated linear baseline correction for the ion drift measurements. These improvements along with the quality-flagging methods of Hairston and Coley (2019) support reproducible and consistent treatment of the full-vector electric field values, which along with the DMSP magnetic perturbations, are used in the PF estimates. Further, we describe a combined binning, averaging, and storage routine for these data, which organizes the observations by location in magnetic coordinates, facilitating future analysis and discovery.

When applying the methods to full-component electric field values we find a 25% overall increase of globally integrated PF compared to PF determined from only the DMSP single-component electric field values. Inter-spacecraft comparisons clearly show that better PF agreement is achieved from the full-component electric field. The near cusp regions, where electric and magnetic field perturbations are constantly responding to the dynamic forcing of the solar wind and IMF component variations, are most affected by the use of the full-component values. Inter-spacecraft PF comparisons using this binned data showed good agreement, with median percent difference of 13% for comparisons between the latest-generation spacecraft (F16 and F18). We anticipate these new PF data products will be useful for future machine learning and empirical modeling efforts as well as model-data comparisons. Access points for the data and data processing routines are provided in the Data Availability Statement.

Data Availability Statement

The data used in this paper (see Table 1) were obtained from NASA Coordinated Data Analysis Web (CDAWeb) https://spdf.gsfc.nasa.gov/pub/data/dmsp/ and from the CEDAR Madrigal database: http://cedar.openmadrigal.org/list. Access to DMSP F15 ion drift Madrigal data was accomplished using Pysat (Stoneback et al., 2021). The binned data products described herein are available on Zenodo (Kilcommons, 2022a). A general purpose Python software library implementing the equal area binning, storage, and retrieval scheme described herein has been published (Kilcommons, 2022b) and is developed at https://github.com/lkilcommons/esabin.

Acknowledgments
LMK was partially supported by AFOSR Award No: FA9550-17-1-0258 and AFOSR MURI Award FA9550-16-1-0364. DJK was partially supported by AFOSR Award No: FA9550-17-1-0258 and by NASA Award 80NSSC20K1784. MH and RC were supported by NASA Grant 80NSSC20K1071.

References

Billett, D. D., McWilliams, K. A., Pakhotin, I. P., Burchill, J. K., Knudsen, D. J., & Martin, C. J. (2022). High-resolution Poynting flux statistics from the Swarm mission: How much is being underestimated at larger scales? *Journal of Geophysical Research: Space Physics*, *127*, e2022JA030573. https://doi.org/10.1029/2022JA030573

Cole, K. D. (1966). Magnetic storms and associated phenomena. *Space Science Reviews*, *5*, 699–770. https://doi.org/10.1007/BF00173103

Cosgrove, R. B., Bahcivan, H., Chen, S., Sanchez, E., & Knipp, D. (2022). Violation of hemispheric symmetry in integrated Poynting flux via an empirical model. *Geophysical Research Letters*, *49*, e2021GL097329. https://doi.org/10.1029/2021GL097329

Cosgrove, R. B., Bahcivan, H., Chen, S., Strangeway, R. J., Ortega, J., Alhassan, M., et al. (2014). Empirical model of Poynting flux derived from FAST data and a cusp signature. *Journal of Geophysical Research: Space Physics*, *119*(1), 411–430. https://doi.org/10.1002/2013JA019105

Dessler, A. J. (1959). Upper atmosphere density variations due to hydromagnetic heating. *Nature*, *184*, 261–262. https://doi.org/10.1038/184261b0

Emmert, J. T., Richmond, A. D., & Drob, D. P. (2010). A computationally compact representation of magnetic-apex and quasi-dipole coordinates with smooth base vectors. *Journal of Geophysical Research: Space Physics*, *115*(A8). https://doi.org/10.1029/2010JA015326

Gary, J. B., Heelis, R. A., & Thayer, J. P. (1995). Summary of field-aligned Poynting flux observations from DE 2. *Geophysical Research Letters*, *22*(14), 1861–1864. https://doi.org/10.1029/95GL00570

Hairston, M., & Coley, W. R. (2019). A Short Introduction to the DMSP SSIES-3 Quality Flags and How to Use Them. *Zenodo*. https://doi.org/10.5281/zenodo.4776161

Huang, C. Y., Huang, Y., Su, Y.-J., Hairston, M. R., & Sotirelis, T. (2017). DMSP observations of high latitude Poynting flux during magnetic storms. *Journal of Atmospheric and Solar-Terrestrial Physics*, *164*, 294–307. https://doi.org/10.1016/j.jastp.2017.09.005

Jacchia, L. G. (1959a). Two atmospheric effects in the orbital acceleration of artificial satellites. *Nature*, *183*, 526–527. https://doi.org/10.1038/183526a0

Jacchia, L. G. (1959b). Corpuscular radiation and the acceleration of artificial satellites. *Nature*, *183*, 1662–1663. https://doi.org/10.1038/1831662a0

Kaeppler, S. R., Knipp, D. J., Verkhoglyadova, O. P., Kilcommons, L. M., & Zhan, W. (2022). Chapter 5—Electromagnetic energy input and dissipation. In Y. Nishimura, O. Verkhoglyadova, Y. Deng, & S.-R. Zhang (Eds.), *Cross-scale coupling and energy transfer in the magnetosphere-ionosphere-thermosphere system* (pp. 301–355). Elsevier. https://doi.org/10.1016/B978-0-12-821366-7.00006-8

Kilcommons, L. M. (2022a). DMSP F15/F16/F18 2011-2014 Binned Poynting Flux Data. [dataset]. Zenodo. https://doi.org/10.5281/zenodo.5829535

Kilcommons, L. M. (2022b). lkilcommons/esabin: V0.2.2. [software]. Zenodo. https://doi.org/10.5281/zenodo.5842038

Kilcommons, L. M., Redmon, R. J., & Knipp, D. J. (2017). A new DMSP magnetometer and auroral boundary data set and estimates of field-aligned currents in dynamic auroral boundary coordinates. *Journal of Geophysical Research: Space Physics*, *122*(8), 9068–9079. https://doi.org/10.1002/2016JA023342

Knipp, D. J., Eriksson, S., Kilcommons, L., Crowley, G., Lei, J., Hairston, M., & Drake, K. (2011). Extreme Poynting flux in the dayside thermosphere: Examples and statistics. *Geophysical Research Letters*, *38*(16). https://doi.org/10.1029/2011GL048302

Knipp, D. J., Kilcommons, L. M., Gjerloev, J., Redmon, R. J., Slavin, J., & Le, G. (2015). A large-scale view of Space Technology 5 magnetometer response to solar wind drivers. *Earth and Space Science*, *2*(4), 115–124. https://doi.org/10.1002/2014EA000057

Knipp, D. J., Kilcommons, L. M., Hairston, M., & Coley, W. R. (2021). Hemispheric asymmetries in Poynting flux derived from DMSP spacecraft. *Geophysical Research Letters*, *48*(17), e2021GL094781. https://doi.org/10.1029/2021GL094781

Knipp, D. J., Matsuo, T., Kilcommons, L., Richmond, A., Anderson, B., Korth, H., et al. (2014). Comparison of magnetic perturbation data from LEO satellite constellations: Statistics of DMSP and AMPERE. *Space Weather*, *12*(1), 2–23. https://doi.org/10.1002/2013SW000987

Laundal, K. M., & Richmond, A. D. (2017). Magnetic coordinate systems. *Space Science Reviews*, *206*(1), 27–59. https://doi.org/10.1007/s11214-016-0275-y

Mosier, S. R., & Gurnett, D. A. (1969). VLF measurements of the Poynting flux along the geomagnetic field with the Injun 5 satellite. *Journal of Geophysical Research*, *74*(24), 5675–5687. https://doi.org/10.1029/JA074i024p05675

Olsson, A., Janhunen, P., Karlsson, T., Ivchenko, N., & Blomberg, L. G. (2004). Statistics of joule heating in the auroral zone and polar cap using Astrid-2 satellite Poynting flux. *Annales Geophysicae*, *22*(12), 4133–4142. https://doi.org/10.5194/angeo-22-4133-2004

Pakhotin, I., Mann, I. R., Xie, K., Burchill, J. K., & Knudsen, D. J. (2021). Northern preference for terrestrial electromagnetic energy input from space weather. *Nature Communications*, *12*(1), 199. https://doi.org/10.1038/s41467-020-20450-3

Rastätter, L., Shim, J. S., Kuznetsova, M. M., Kilcommons, L. M., Knipp, D. J., Codrescu, M., et al. (2016). GEM-CEDAR challenge: Poynting flux at DMSP and modeled Joule heat. *Space Weather*, *14*(2), 113–135. https://doi.org/10.1002/2015SW001238

Rich, F. J., Bono, J. M., Burke, W. J., & Gentile, L. C. (2007). A space-based proxy for the Dst index. *Journal of Geophysical Research: Space Physics*, *112*(A5), A05211. https://doi.org/10.1029/2005JA011586

Stoneback, R. A., Burrell, A. G., Klenzing, J., & Depew, M. D. (2018). PYSAT: Python satellite data analysis toolkit. *Journal of Geophysical Research: Space Physics*, *123*(6), 5271–5283. https://doi.org/10.1029/2018JA025297

Stoneback, R. A., Klenzing, J., Burrell, A. G., Pembroke, A., Spence, C., Depew, M., et al. (2021). pysat/pysat: V3.0.1. [software]. Zenodo. https://doi.org/10.5281/zenodo.5142690

van der Meeren, C., Laundal, K. M., Burrell, A. G., Starr, G., Reimer, A. S., & Morschhauser, A. (2021). aburrell/apexpy: Apexpy version 1.1.0. [software]. Zenodo. https://doi.org/10.5281/zenodo.4585641

Weimer, D. R. (2005). Improved ionospheric electrodynamic models and application to calculating joule heating rates. *Journal of Geophysical Research: Space Physics*, *110*(A5). https://doi.org/10.1029/2004JA010884